

Salt Fog Corrosion Testing of Al-Y-Co based Nanocrystalline and Amorphous Coatings Produced by Atmospheric Plasma Spray

Y. Kato, D.C. Van Aken

Department of Materials Science and Engineering, University of Missouri-Rolla, Rolla, Missouri, USA

Abstract

Alloys based upon the Al-Y-Co system were atmospheric plasma sprayed (APS) to produce amorphous coatings with varying amounts of nanocrystalline precipitates of aluminum. All of the coatings produced in this study were deposited on 7075-T651 plate. $\text{Al}_{91}\text{Y}_4\text{Ni}_4\text{Co}_1$ and $\text{Al}_{91}\text{Y}_4\text{Co}_5$ alloys produced a mixed microstructure of metallic glass and nanocrystalline aluminum with grain diameters between 10 and 15 nm. In contrast, coatings of $\text{Al}_{81}\text{Y}_{12}\text{Ni}_5\text{Co}_2$, $\text{Al}_{85}\text{Y}_8\text{Ni}_5\text{Co}_2$, and $\text{Al}_{89}\text{Y}_4\text{Co}_5\text{Mo}_2$ were almost entirely amorphous. Glass forming ability and hardness of the coatings increased in proportion to the yttrium content. Salt fog corrosion tests were performed in accordance with ASTM B117-03. Corrosion performance of the coating was limited by coating permeation and subsequent attack of the 7075-T651 substrate. Improved corrosion performance was obtained using a silicone-based sealant to reduce coating permeation. Densification of the coating, using a CO_2 laser, produced a crystalline coating with poor corrosion resistance.

Introduction

Amorphous metallic alloys are of growing interest for application as corrosion resistant coatings and as a replacement for hard chrome plating. Unlike crystalline metals, the amorphous structures are free from defects, such as grain boundaries, dislocations and long-range chemical segregation, which typically are associated with the formation of galvanic corrosion cells. Formation of metallic glass requires rapid quenching (generally, $> 10^5$ K/sec) to produce significant undercooling to reach the glass forming temperature. Recent research has shown that thermal spray processes are capable of producing metastable and amorphous coatings.^{1,2,3,4} In a study by Kato and Van Aken it was shown that undercooling on the order of more than 200 °C can be achieved for an Al-Ge eutectic alloy using atmospheric plasma spray.⁴

Kishitake et al. investigated corrosion resistance of $\text{Fe}_{70}\text{Cr}_{10}\text{P}_{13}\text{C}_7$ (in at%) glass forming alloy using three thermal spray methods: low pressure plasma spray (LPPS), high-velocity oxy-fuel (HVOF) and high energy plasma spray (HPS).¹ As-sprayed coatings exhibited varying degrees of crystallinity and the degree of coating crystallization increased with increasing heat energy of the process. Coatings produced

by LPPS were entirely amorphous whereas the higher heat generated by HVOF and HPS produced mixed microstructures of amorphous and crystalline phases in the coating. Anodic polarization studies of the coatings in 1N HCl showed the best corrosion resistance for the amorphous coating, which was produced by LPPS. The measured current densities were about three orders of magnitude lower than that observed for 316 stainless steel when measured at the same potential. HVOF and HPS coatings with mixed microstructures were less corrosion resistant, but were still more corrosion resistant than the 316 stainless steel. Addition of Mo to the coating alloy also increased the glass forming ability and it became possible to produce amorphous coatings using HVOF. The corrosion resistance of a $\text{Fe}_{61}\text{Cr}_{9.4}\text{Mo}_9\text{P}_{12.6}\text{C}_8$ alloy applied by HVOF was comparable to the $\text{Fe}_{70}\text{Cr}_{10}\text{P}_{13}\text{C}_7$ alloy¹ applied by LPPS.²

The corrosion resistance of aluminum-based glasses appears to be less dependent upon degree of crystallinity. Nanocrystalline microstructures produced in the bulk glass forming aluminum alloys $\text{Al}_{87}\text{Y}_{4.3}\text{Ni}_{8.7}$ and $\text{Al}_{90}\text{Fe}_5\text{Gd}_5$ exhibited comparable corrosion resistance with that of the amorphous state.⁵

In the work presented here, the corrosion resistance of Al-based nanocrystalline and amorphous coatings produced using atmospheric plasma spray (APS) was investigated by salt fog tests. The primary goal of this work was to determine the influence of coating macrostructure, alloy composition and microstructure on corrosion resistance of APS coatings.

Experimental Procedure

Four alloy compositions were produced by arc melting 99.99% purity elements with a Y-Al master alloy of 99.9% purity to produce alloys with compositions in atomic percent of $\text{Al}_{91}\text{Y}_4\text{Co}_5$, $\text{Al}_{81}\text{Y}_{12}\text{Ni}_5\text{Co}_2$, $\text{Al}_{85}\text{Y}_8\text{Ni}_5\text{Co}_2$, and $\text{Al}_{89}\text{Y}_4\text{Co}_5\text{Mo}_2$. An $\text{Al}_{91}\text{Y}_4\text{Ni}_4\text{Co}_1$ alloy was also obtained in the form of an amorphous powder. Arc melted ingots were subsequently pulverized using a saucer mill (model LM1 by Labtechnics, Australia) to produce powders suitable for plasma spraying. Powders were sieved with a 325 mesh (45 μm) standard testing sieve and larger powders were returned to the mill for further reduction.

Solidus temperatures for the alloys were determined by differential thermal analysis (DTA) of the saucer-milled

powders. DTA experiments were conducted under flowing argon gas and a temperature ramp rate of 10K/min. was used. Each alloy exhibited an endothermic onset temperature between 636 and 639°C indicating the solidus temperature of each alloy was near a eutectic reaction. The $Al_{91}Y_4Ni_4Co_1$ was thought to be very close to a quaternary eutectic composition since the melting range was the smallest of the alloys tested.

Aluminum alloy 7075-T651 plates (2.5 cm x 7.5 cm x 0.64 cm) were grit blasted using silica sand to produce a surface roughness of 3.6 μm R_a (average roughness) and 24 μm R_z (average peak-to-valley) prior to APS coating. A Sulzer-Metco 9 MB plasma gun mounted on a 6-axis robot was utilized to apply 200 to 250 μm thick coatings. Spray parameters were fixed at 14.4 kW input energy, 47.2 lpm argon flow rate, 8 cm spraying distance, and 1.5 cm spray-scan spacing. Although hydrogen was also used to increase the plasma heat, the amount of gas flow did not register on the rotometer.

APS coating quality was found to depend upon the traverse direction of the robot with respect to the external powder injector tube position. For the stationary gun the metal deposition was located at the 9 o'clock position (as viewed from behind the gun) when the powder injector tube was attached at the 1 o'clock position. A dense coating was produced when the gun was traversed towards the deposit (9 o'clock). However, a porous coating, containing large amounts of unmelted powders resulted when the gun was traversed in the opposite direction (3 o'clock). Thus, sweeping the plasma gun in a single direction over the substrate produced dense coatings and moving the plasma gun in both directions produced less dense coatings. In this manner, specimens with high and low density were produced. Furthermore, the crystallinity of the coatings was minimized by maintaining the substrate temperature below 60°C. This required that the coating be deposited in multiple passes of approximately 10 to 30 μm in thickness each with subsequent cooling between passes to produce a final coating thickness between 200 and 250 μm .

Three post-spray coating treatments were performed to investigate the influence of coating permeability and microstructure on corrosion resistance. Coatings were sealed with a silicone-based organic polymer ('Permeate' produced by the D&D Corporation, Japan). After curing the sealant for 24 hours, the top film was removed with 400-grit sandpaper until a gloss metallic surface finish was produced. Consolidation of the plasma sprayed coating was also performed using a CO₂ laser. The laser scanning parameters were 500 W beam energy, 1.5 mm laser diameter, 25.4 cm/min. traverse speed, 0.5 mm laser overlap, and 10.6 μm wavelength. Six scan rows were made per cycle to keep the untreated portion of the specimen below 100 C°. In this scanning program, one half of each specimen surface area was treated and the other half was left untreated.

Microstructural characterization was performed using scanning electron microscopy and powder X-ray diffraction (XRD). Cross-sections of the coatings were prepared using standard metallographic techniques. Coating crystallinity was investigated using a Phillips PW3040 diffractometer with Cu K_{α} radiation of 1.542 Å. Coatings were ground to less than 75 μm using mortar and pestle. Nanocrystalline grain diameters of the $Al_{91}Y_4Ni_4Co_1$ and $Al_{91}Y_4Co_5$ coatings were determined by fitting the Scherrer equation to 111, 200, and 220 diffraction peaks of aluminum using the software JADE (Materials Data Incorporated). Instrumental error of the diffraction profile was corrected using a standard powder diffraction pattern from NIST 640B silicon powder.

Qualitative corrosion resistance of coatings, with the exception of $Al_{81}Y_{12}Ni_5Co_2$, was examined using a salt-fog chamber in accordance with ASTM B117-03. The degree of resistance was determined by visual examination to compare unaffected coating surface area before and after the test. Corrosion specimens were first masked with electrical tape to produce an area of exposure that measured 1.8 cm x 6 cm. The masking was then sealed with an acrylic paint. Specimens were placed on a Nylon rack in the vertical position. All corrosion specimens except the sealed specimens were tested in a salt-spray chamber for 96 hours. The sealed specimens (with silicone-based organic polymer) were tested for 168 hours.

Results

Coating macro and microscopic structures were found to vary with application technique. Secondary electron images of the coating surfaces and that of metallographically prepared cross-sections are shown in Fig.1. The porous coating structures shown in Fig. 1(a) and (c) were produced by traversing the plasma gun in two directions as described in the experimental procedures. Spraying only in one direction produced a denser coating (see Fig. 1(b) and (d)) and the coating surface appeared brighter due to a reduction in the number of unmelted powders in the coating.

Microstructures of the porous coatings, as shown in Fig. 2(a), show a large amount of un-melted or partially melted powders in the coating. These un-melted powders consist of many angular intermetallic particles (brighter contrast because of the high yttrium content), which were also observed in the milled powders. The microstructure of the denser coating is nearly featureless, but may contain an occasional intermetallic particle that is similar to that observed in the milled or unmelted powders. Intermetallics in the dense coating tend to be smaller and this may indicate that the splat was not entirely liquid upon impact. It should be noted that there is a contrast variation between the various lamellar splats making up the dense coating as shown in Fig. 2(b). Qualitative chemical analysis using energy dispersive spectroscopy reveals that the contrast difference is associated with differences in yttrium content with higher yttrium containing splats appearing brighter.

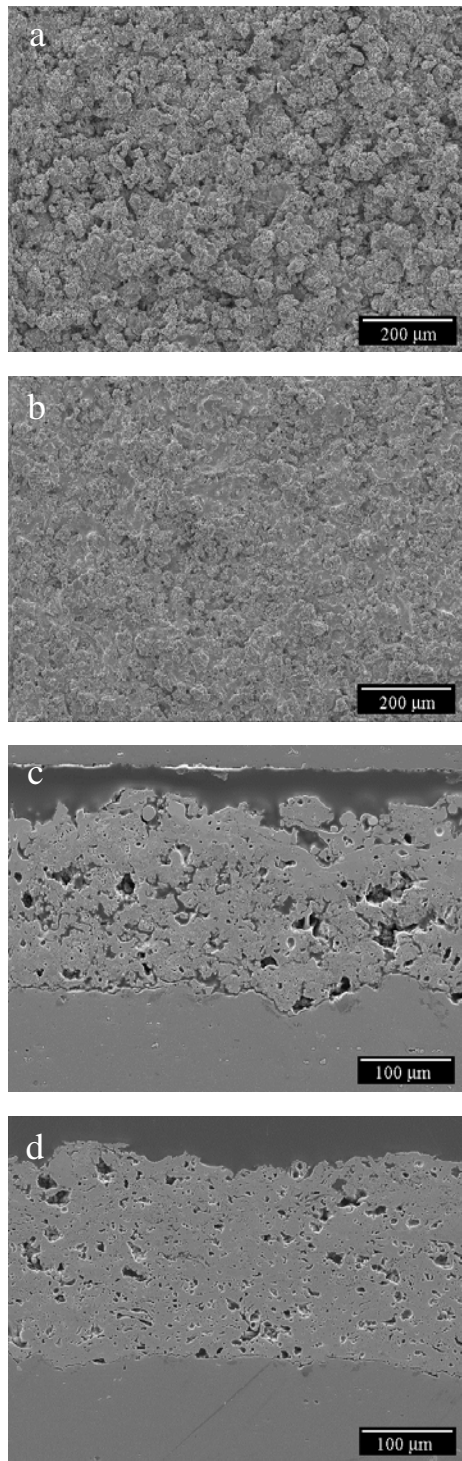


Figure 1. Secondary electron microscope images of $Al_{85}Y_8Ni_5Co_2$ coating surface and cross-section. Unmelted spherical powders observed profusely in coating surface (a) were eliminated in the coating (b). Cross-section images also show the difference in the amount of porosity in each coating. Some micropores in (c) are filled with epoxy. Weak bonding of the porous coating onto the 7075 alloy substrate is indicated by the presence of epoxy at the interface.

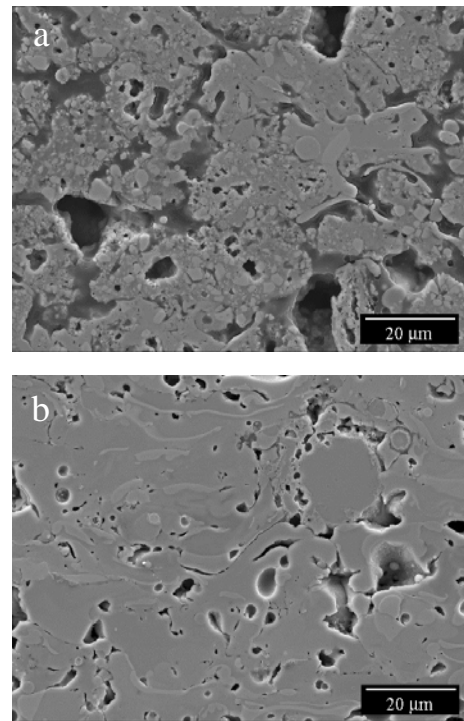


Figure 2. Secondary electron images of the of $Al_{85}Y_8Ni_5Co_2$ coating showing the difference in microstructure between coatings produce by traversing the plasma gun in two directions (a) and in a single direction (b). The coating shown in (a) contains many un-melted powders while the coating in (b) shows a well defined lamellar splat morphology.

Differential thermal analysis (DTA) of saucer-milled powders revealed large endothermic peaks between 636 and 639 °C indicating that each alloy investigated was near in composition to a eutectic reaction. The $Al_{91}Y_4Ni_4Co_1$ alloy was closest in composition to the eutectic since the area of the endothermic peak was the largest and the melting range above the eutectic isotherm was the smallest of the five alloys investigated. However, the $Al_{91}Y_4Ni_4Co_1$ alloy still has a large melting range of at least 150 °C (see Fig.3).

Powder x-ray diffraction patterns of the five alloys (dense coatings only) revealed both amorphous and nanocrystalline structures. In general, the coatings became less crystalline as the amount of yttrium increased in the alloy and $Al_{81}Y_{12}Ni_5Co_2$ had the highest glass forming ability. Coatings of $Al_{85}Y_8Ni_5Co_2$ and $Al_{89}Y_4Co_5Mo_2$ had lower glass forming ability. $Al_{91}Y_4Ni_4Co_1$ and $Al_{91}Y_4Co_5$ coatings contained nanocrystalline aluminum grains with grain diameters between 10 and 15 nm. Un-melted powders were also present in the amorphous materials and were differentiated from the nanocrystalline structures by the absence of peak broadening. The 111 and 200 reflections shown in Fig. 4(a) are most likely from un-melted powders in the coating. In contrast, Fig. 4(b) shows the broadening effects of the nanocrystalline α -Al particles on the diffraction patterns. In addition, there is evidence of an amorphous structure superposed on the background of the diffraction pattern in Fig. 4(b).

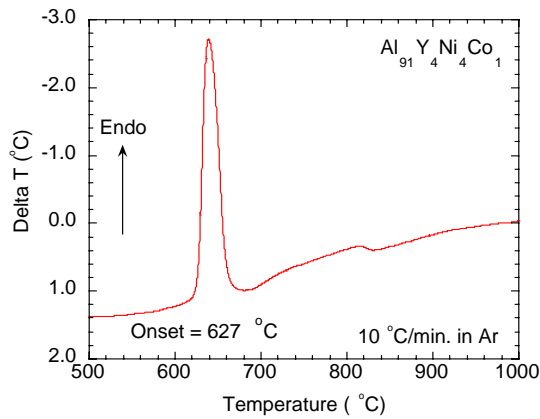


Figure 3. DTA scan of saucer-milled $\text{Al}_{91}\text{Y}_4\text{Ni}_4\text{Co}_1$ powder used for APS coating showing a large endothermic reaction believed to be a eutectic isotherm. The shallow endothermic reaction, indicative of slow reaction kinetics or a steep liquidus for the Al_3Y and Ni-rich compounds.

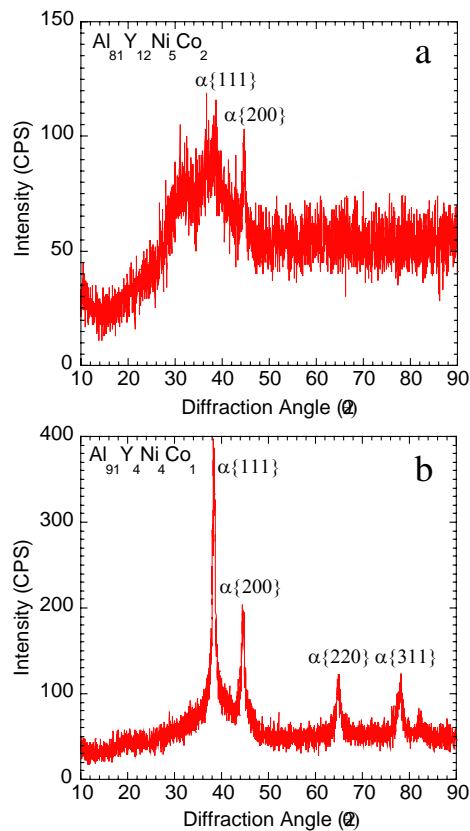


Figure 4. The amount of amorphous phase is increased by substitution of yttrium and molybdenum for aluminum. Absence of the 220 and 311 α -aluminum diffraction peaks in (a) suggests that the $\text{Al}_{81}\text{Y}_{12}\text{Ni}_5\text{Co}_2$ coating is nearly all amorphous with the exception of un-melted powders, which are always present in APS coatings. Figure (b) shows a diffraction pattern from a nanocrystalline coating superposed upon a broad diffraction maxima associated with an amorphous structure.

Decomposition of the amorphous coating structure was studied using differential scanning calorimetry (DSC). A temperature ramp rate of $40\text{ }^\circ\text{C}/\text{min}$ produced exothermic phase transformations that were absent when the specimen was subsequently reheated. The DSC results from the nanocrystalline $\text{Al}_{91}\text{Y}_4\text{Ni}_4\text{Co}_1$ coating is shown in Fig. 5. The exothermic peaks shown correspond to the devitrification of Y-rich amorphous phase.⁶⁻¹⁹

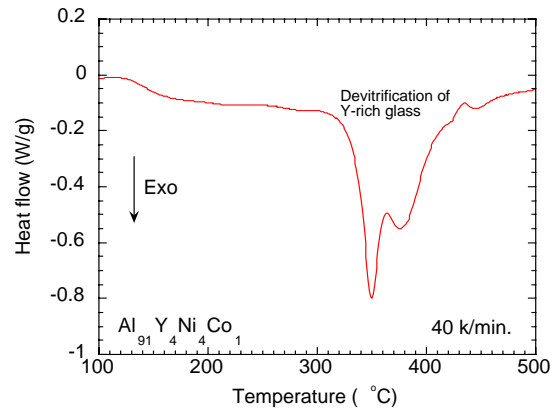


Figure 5. A calorimetry study of the $\text{Al}_{91}\text{Y}_4\text{Ni}_4\text{Co}_1$ coating showing the decomposition or devitrification of the yttrium-rich glass.

The as-sprayed coating hardness was measured by Vickers indentation using a 200 gram load. The measured hardness is shown in Table 1. The results indicate that the coating hardness increased in proportion to the yttrium content. However, the substitution of molybdenum appears to be more effective in increasing the hardness on a per atom basis than yttrium.

Table 1. Average Vickers hardness value measured on a polished coating surface. The uncertainty in the hardness measurements reflects the sample standard deviation with a population of 20 measurements.

Alloy	Vickers Hardness
$\text{Al}_{81}\text{Y}_{12}\text{Ni}_5\text{Co}_2$	401 ± 25
$\text{Al}_{89}\text{Y}_4\text{Co}_5\text{Mo}_2$	314 ± 14
$\text{Al}_{85}\text{Y}_8\text{Ni}_5\text{Co}_2$	242 ± 17
$\text{Al}_{91}\text{Y}_4\text{Co}_5$	157 ± 19
$\text{Al}_{91}\text{Y}_4\text{Ni}_4\text{Co}_1$	137 ± 12

Salt fog testing revealed that the $\text{Al}_{91}\text{Y}_4\text{Co}_5$ coating exhibited the best corrosion resistance of the alloys investigated regardless of coating structure and post spray treatment. Alloys containing nickel such as $\text{Al}_{85}\text{Y}_8\text{Ni}_5\text{Co}_2$ and $\text{Al}_{91}\text{Y}_4\text{Ni}_4\text{Co}_1$ exhibited very poor corrosion resistance with early development of corrosion pits. Substitution of cobalt or molybdenum for the nickel improved the corrosion resistance of the coating. It was found during the corrosion test that almost all of the coatings were contaminated with copper powder from a prior APS experiment. Presence of copper in the coating was identified by a characteristic reddish brown spot with a white gelatin-like corrosion by-product surrounding the corrosion pit. Rapid attack of the 7075-T651 substrate was usually observed near the copper initiated pit. However, these copper contaminates were usually isolated and left large areas of the test specimen available for observation of the coating corrosion behavior.

In general the APS coatings behaved as corrosion barrier coatings and permeability of the coating was the most important factor in determining the salt fog corrosion resistance. Rapid pit formation and subsequent delamination of the coating was observed in the porous coatings. Delamination was usually observed as a blistering of the coating around the corrosion pit. The extent of coating delamination could only be determined in metallographically prepared cross-sections and was usually much more extensive than the macroscopic blistering of the coating. The dense coatings also exhibited pit formation, but the pit density was lower. In general, the coatings require a silicone sealant to prevent the rapid pit formation. Metallographically prepared cross-sections revealed that the silicone penetrates to a depth of 100 μm . Results from the 168 hour salt fog test of silicone sealed coatings are shown in Fig. 6. Despite the presence of copper, it can clearly be seen that the $\text{Al}_{91}\text{Y}_4\text{Co}_5$ and $\text{Al}_{89}\text{Y}_4\text{Co}_5\text{Mo}_2$ coatings show superior pitting resistance relative to the nickel containing coatings. One of the $\text{Al}_{91}\text{Y}_4\text{Co}_5$ coatings was free from copper-induced pit formation.

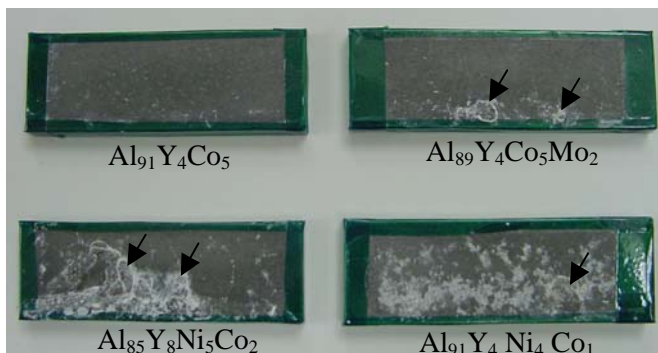


Figure 6. Optical image of the 168 hour salt fog tested specimens. These specimens were prepared with dense coatings and subsequently silicone sealed. Copper-induced pits are indicated by arrows in the figure.

Coating densification was also performed by laser melting the APS coating, however, the coating was transformed to a crystalline structure consisting of coarse intermetallic compounds (see Fig. 7(a)). Surface melting reduced the porosity in the fusion zone, but also produced minor microcracking. A comparison of corrosion attack among the four alloy compositions showed that the laser treated surface was less corrosion resistant (higher pit density) than the as-sprayed coating (see Fig. 7(b)).

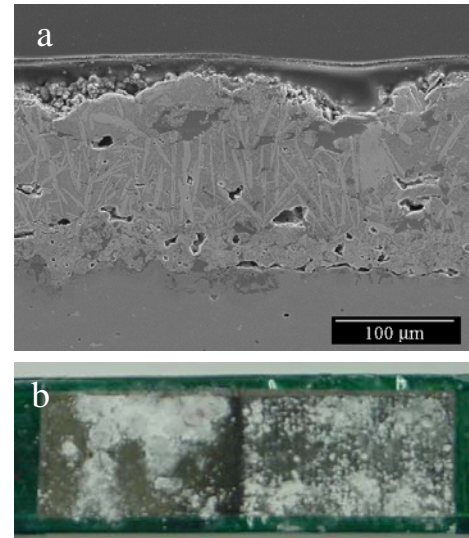


Figure 7. (a) A secondary electron image of the laser-treated coating showing reduced porosity in the coating surface and an acicular morphology of intermetallic particles indicating a crystalline coating microstructure. (b) Optical images of the salt fog tested specimens after 96 hours. The right half of the specimen was laser treated and shows a uniform pitting attack of the coating. The left half of the specimen was in the as-sprayed condition and heat-affected condition, but it was corroded to the same degree as as-sprayed coating.

Discussion

It has been shown in this study that amorphous and nanocrystalline coatings can be produced by atmospheric plasma spraying Al-Y-Co-based alloys. Furthermore, the glass forming ability and coating hardness increases as the yttrium content of Al-Y-Ni-Co based alloys is increased. Similar trends in glass forming ability and hardness were reported for the bulk glass forming $\text{Al}_{93-x}\text{Y}_x\text{Ni}_5\text{Co}_2$ alloys when x varied between 8 and 12 atomic percent.²⁰ The hardness of the bulk amorphous alloys was reported to increase from 340 to 400 HV as the yttrium content increased from 8 to 12 atomic percent. Previous studies on bulk glass forming aluminum alloys have shown that an increase in hardness is observed upon devitrification of the glass to form a nanocrystalline microstructure.^{9,10,14} However, the coating that exhibited the highest hardness values in the present study was amorphous as shown by the powder x-ray diffraction patterns. These coatings exhibited extremely high hardness

with the $Al_{81}Y_{12}Ni_5Co_2$ APS coating hardness being in excess of 400 HV and the $Al_{89}Y_4Co_5Mo_2$ coating hardness in excess of 300 HV. It was also noted that the amorphous coating alloys became more prone to spalling off the substrate as the coating thickness increased beyond 200 μm . The nature of the spall indicated that the coating was in compression. An interesting aspect of forming the amorphous coating is that stress relaxation by dislocation and/or grain boundary creep would not be possible. Thus, high residual stresses may be retained in the amorphous APS coatings.

Results of the salt fog tests show that select amorphous and nanocrystalline coatings are effective corrosion barriers when the coating permeability is reduced by a silicone sealant. However, alloys containing nickel are attacked regardless of yttrium content, the crystallinity of the coating or the addition of a sealant. The most corrosion resistant coatings investigated were the $Al_{91}Y_4Co_5$ and $Al_{89}Y_4Co_5Mo_2$ compositions. However, when these alloys were laser surface melted the corrosion resistance was drastically reduced. The loss in corrosion resistance is believed to be a result of the microstructural changes induced by the laser processing, which produced a crystalline coating consisting of aluminum and intermetallic compounds. Similar observations were observed for the sealed porous coatings that contained a high density of un-melted powders.

Unsealed coatings formed pits locally where the coating density allowed concentration cells to be formed. Coating failure was accelerated when the corrosion pit enlarged to reach the 7075-T651 substrate and preferential corrosion of the substrate produced voluminous corrosion products, which manifested as blisters on the coating surface. The extent of the corrosion could only be observed in metallographic cross-sections of the tested coating. Typically, the corrosion extended beyond the diameter of the blister.

Conclusions

Atmospheric plasma spray of Al-Y-Co based alloy powders has been shown to produce amorphous and nanocrystalline coatings. These coatings can be effective corrosion barriers provided the coating permeability is reduced by the application of a silicone sealant. Nickel additions to the Al-Y-Co base alloy are detrimental to the corrosion resistance regardless of yttrium content. However, Al-Y-Co and Al-Y-Co-Mo based coatings show potential for use as wear and corrosion resistant amorphous coatings. Coating hardness and glass forming ability can both be increased by substitution of yttrium for aluminum and a coating hardness in excess of 400 HV is possible.

Acknowledgements

This work was supported in part by the University of Missouri Research Board and the Army Research Laboratory (ARL).

The ARL technical monitor was Dr. Walter Roy. The authors are also grateful to Dr. David Bowden of the Boeing Company Advanced Manufacturing Research and Development Group for many stimulating conversations concerning the Al-Y-Ni-Co system. Equipment and instrumentation support from NSF under contract DMI-0116158 is gratefully acknowledged as is the D&D Corporation for supplying the silicone sealant.

References

1. K. Kishitake, H. Era, and F. Otsubo, J. of Thermal Spray Technology, 5(4), 476-482 (1996).
2. K. Kishitake, J. of Japan Thermal Spraying Society, 40(2), 70-74 (2003).
3. K. Kishitake, H. Era, and F. Otsubo, J. of Japan Thermal Spraying Society, 32(3), 24-28 (1995).
4. Y. Kato and D.C. Van Aken, Scripta Materialia, 50, 445-448 (2004).
5. J.E. Sweitzer, J.R. Scully, R.A. Bley, and J.W.P. Hsu, Electrochem. and Solid-State Letters, 2(6), (1999) 267-270.
6. A. Inoue, Mat. Sci. and Eng., A179/180, 57-61 (1994).
7. Z.C. Zhong and A.L. Greer, International J. of Non-Equilibrium Processing, 11, 35-53 (1998).
8. A.L. Greer, Met. and Mat. Trans. A, 27A, 549-555 (1996).
9. A.L. Greer, Z.C. Zhong, X.Y. Jiang, K.L. Rutherford, and I.M. Hutchings, Chem. and Phys. of Nanostructures and Related Non-Equilibrium Materials, 3-12 (1997).
10. Z.C. Zhong, X.Y. Jiang, A.L. Greer, Mat. Sci and Eng., A226-228, 531-535 (1997).
11. Z.C. Zhong and A.L. Greer, J. of Mater. Sci. Technology, 12, 1-6 (1996).
12. X.Y. Jiang, Z.C. Zhong, and A.L. Greer, Mat. Sci. and Eng. A226-228, 789-793 (1997).
13. X.Y. Jiang, Z.C. Zhong, and A.L. Greer, Philosophical Mag. B, 76, 419-423 (1997).
14. J. Latuch, A. Kokoszkiwicz, A. Calka, Materials Science Forum, 235-238, 309-314 (1997).
15. J.H. Perepezko and R.J. Hebert, JOM, March, 34-42 (2002).
16. R.I. Wu, G. Wilde, and J.H. Perepezko, Mat. Sci. and Eng., A301, 12-17 (2001).
17. J.H. Perepezko, R.I. Wu, R. Hebert, and G. Wilde, Mat.Res. Symp. Proc. 644, L4.7.1-L4.7.11 (2001).
18. N. Bassin, C.S. Kiminami, M.J. Kaufman, J. of Non-crystalline Solids, 273, 271-276 (2000).
19. A.P. Tsai, T. Kamiyama, Y. Kawamura, A. Inoue, and T. Masumoto, Acta Mater., 45(4), 1477-1487 (1997).
20. A. Inoue, N. Matsumoto, and T. Masumoto, Mat. Transactions, JIM, 31, 493-500 (1990).
